Research Article | Vol. 12, No. 1 / 1 January 2021 / Biomedical Optics Express 604
Biomedical Optics EXPRESS

Characterization of fibrillar collagen isoforms in infarcted mouse hearts using second harmonic generation imaging

SUSHANT P. SAHU,[1] QIANGLIN LIU,[2] ALISHA PRASAD,[3] SYED MOHAMMAD ABID HASAN,[3] QUN LIU,[4] MARIA XIMENA BASTIDAS RODRIGUEZ,[4] ORNA MUKHOPADHYAY,[5] DAVID BURK,[6] JOSEPH FRANCIS,[7] SUPRATIK MUKHOPADHYAY,[4] XING FU,[2,8] AND MANAS RANJAN GARTIA[3,9]

[1]*Department of Chemistry, University of Louisiana at Lafayette, Lafayette, LA 70504, USA*
[2]*LSU AgCenter, School of Animal Sciences, Louisiana State University, Baton Rouge, LA 70803, USA*
[3]*Department of Mechanical and Industrial Engineering, Louisiana State University, Baton Rouge, LA 70803, USA*
[4]*Department of Computer Science, Louisiana State University, Baton Rouge, LA 70803, USA*
[5]*Baton Rouge Magnet High School, Baton Rouge, LA 70806, USA*
[6]*Shared Instrumentation Facility and Pennington Biomedical Research Center, Baton Rouge, LA 70808, USA*
[7]*Comparative Biomedical Sciences, School of Veterinary Medicine, Louisiana State University, Baton Rouge, LA 70803, USA*
[8]*xfu1@agcenter.lsu.edu*
[9]*mgartia@lsu.edu*

Abstract: We utilized collagen specific second harmonic generation (SHG) signatures coupled with correlative immunofluorescence imaging techniques to characterize collagen structural isoforms (type I and type III) in a murine model of myocardial infarction (MI). Tissue samples were imaged over a four week period using SHG, transmitted light microscopy and immunofluorescence imaging using fluorescently-labeled collagen antibodies. The post-mortem cardiac tissue imaging using SHG demonstrated a progressive increase in collagen deposition in the left ventricle (LV) post-MI. We were able to monitor structural morphology and LV remodeling parameters in terms of extent of LV dilation, stiffness and fiber dimensions in the infarcted myocardium.

© 2020 Optical Society of America under the terms of the OSA Open Access Publishing Agreement

1. Introduction

Myocardial Infarction (MI) is major source of mortality (~ 15%) around the world eventually resulting in heart failure [1,2]. Despite extensive research and development in associated treatment therapies, fatality rates exceed > 40% amongst rehospitalized heart patients [1,2]. For instance, in the United States alone, heart failure affects ~ 6 million people, responsible for the death of > 300 000 people per year, and is directly accountable for > $40 billion in healthcare costs [1,2]. Fibrosis is essential for the ventricular remodeling post MI [3]. In the infarcted heart, firm fibrous tissue created due to natural healing process, is needed for the chamber to continue pumping blood effectively [4]. However, non-optimal healing and repair process of the tissues may lead to adverse ventricular remodeling and unfavorable outcome [5]. Therefore, a better understanding of the mechanism behind fibrosis may lead to new therapeutics for controlling fibrosis to improve survival after MI.

There are two types of fibrosis in cardiac tissues: replacement or reparative fibrosis and reactive fibrosis. In reparative fibrosis, the dead cardiomyocytes are replaced by collagen fibers. The reactive fibrosis is characterized by growth of collagen fibers in the perivascular and interstitial

#410347 https://doi.org/10.1364/BOE.410347
Journal © 2021 Received 21 Sep 2020; revised 14 Dec 2020; accepted 14 Dec 2020; published 23 Dec 2020

Biomedical Optics EXPRESS

spaces of the cardiac tissues even without the loss of cardiomyocytes [6]. Although both type of fibrosis can be seen in acute MI, reactive fibrosis is a distinctive feature of chronic heart diseases and can be seen in hypertensive cardiac disease, diabetic cardiomyopathy, aortic valve stenosis as well as hypertrophic heart conditions [7,8]. The total collagen content in the heart is not static and it is estimated that collagen is synthesized and degraded at a rate of 5% per day [9]. Hence, there is delicate balance between the synthesis and degradation of collagen in the myocardium. Any dysregulation due to various cardiomyopathies disturb the balance and leads to accumulation of collagen causing fibrosis. The tissues in myocardial fibrosis are mainly composed of collagen type I (highly cross-linked fibers with large diameter) and collagen type III (non-cross-linked fibers with small diameter) [10]. Due to the difference in the biophysical properties of these fibers, a small change in the ratio of collagen type I to type III may alter the stiffness of myocardium leading to impaired diastolic and systolic function [7,11]. The severity of fibrosis may be a good indicator of the effectiveness of long-term heart failure therapy such as beta-blocker [12]. Therefore, developing a robust methodology to assess cardiac fibrosis is important for determining the proper therapy for the patients as well as establishing an accurate prognosis for heart failure.

The current gold standard for the diagnosis of myocardial fibrosis is using histopathological analysis of the cardiac tissue obtained from endomyocardial biopsy [13,14]. Endomyocardial biopsy is considered to be safe with transient complication rate of $< 0.5\%$ and cardiac perforation risk of $< 0.05\%$ [15]. The quantification of collagen in the fixed tissues are generally performed using light microscopy imaging of histological sections while staining them with dyes such as picrosirius red [16–18] or Masson's trichrome [19,20] or fluorescence immunolabel [21]. However, the results from these analysis are subjective, depends on the experience and interpretation skills of the users, prone to staining errors, and may lead to sampling error if several tissue samples are not used (due to the patchy distribution of collagen especially in reactive fibrosis). Since these tissue staining methods are irreversible, the same tissue section cannot be utilized for further analysis. Other clinical approach to visualize cardiac fiber includes late gadolinium enhanced magnetic resonance imaging (LGE-MRI) [22], magnetic resonance diffusion tensor imaging (MR-DTI) [23], and ultrasound (echocardiography) [24]. However, with spatial resolution of $\sim$ 0.1–1 mm, current clinical imaging modalities lack microscopic resolution and molecular specificity [25,26].

Multi-modal non-linear imaging such as two-photon and second harmonic generation (SHG) can overcome some of the potential pitfalls of both traditional histology (subjectivity, unusable tissue) and clinical imaging (lack of specificity/ spatial resolution). The autofluorescence signal generated from the cardiac tissues due to two-photon excitation can be utilized to image elastin, and reduced nicotinamide adenine dinucleotide (NADH) without using any exogenous proteins or dyes [27–29]. Compared to fluorescence imaging (which involves absorption of photons), SHG imaging leads to minimal phototoxicity and photobleaching as SHG process is due to the induction of polarization and not an absorption mode [30]. Since its first demonstration to image collagen structures [31], SHG microscopy has emerged as a powerful tool to image extracellular matrices (ECMs) and cellular architectures of thicker tissue (several hundreds of microns thick) samples in their natural environments [30,32–36], to image single molecule [37], to perform super-resolution localization [38] and also in nanophotonics research [39]. Moreover, SHG is label-free, non-invasive, non-destructive, non-absorptive process hence it's a non-photobleaching imaging tool with high 3D depth of penetration for imaging thick tissue specimens [32,34–36]. However, SHG has never been utilized to systematically study the progression of fibrosis after MI. In our previous work, we estimated heart risk factor from the SHG images of the whole heart tissues using generative adversarial networks (GAN); however the computational framework did not distinguish the collagen isoforms [40]. In this paper, we utilized back-propagating SHG coupled with correlative immunofluorescence imaging techniques to characterize collagen

Biomedical Optics EXPRESS

structural isoforms (collagen type I and type III) and to study time-dependent progression of cardiac fibrosis after MI injury in the infarcted myocardium of mouse hearts. We were able to visualize the spatially resolved 2D structural organization of collagen, tissue morphological features as well as post-MI ventricular remodeling and ECM architecture in heart tissues with high spectral specificity and sensitivity. By using simultaneous acquisition of SHG light scattering from collagens and immunofluorescence staining of type I and type III collagen isoforms in the infarcted scar zone, we were able to study the kinetics of collagen I and III progression in the LV scar tissue following MI. Traditional picrosirius red and immunofluorescence imaging of antibodies labeled tissues were performed to validate the SHG results. We also analyzed the fiber length, width, number of fibers and arrangement of fibers quantitatively during the progression of fibrosis after MI in the epicardium, septum and endocardium. Furthermore, utility of these imaging methods and analyses in this study will be valuable for the assessment of therapeutic approaches aimed at understanding ECM structure-function relationships in MI induced heart failure model.

2. Experimental section

2.1. Infarcted mouse hearts

10 weeks old male C57BL/6 mice (Jackson laboratory) (n = 55) were used in this study. All animal experiments were approved by the Institutional Animal Care and Use Committee (IACUC) at LSU. MI was induced in mice by permanent left coronary artery (LAD) ligation [21,41]. Briefly, isoflurane was used for anesthetizing the mice followed by a left lateral thoracotomy procedure to perform ligation. For managing the pain due to the surgical procedures, mice were given Carprofen (5 mg/kg body weight) by s.c. injection. The mice were sacrificed at time periods of 1–7, 14, 21, and 28 days after MI. Cardiac tissue specimens were obtained and processed following the procedures reported previously [21]. Echocardiography was performed using a Toshiba SSA770 system. Only mice with successful LAD ligation were included in analysis.

2.2. Tissue processing

4% paraformaldehyde (3.5 hrs) were used for fixing the heart samples. After fixing several washing steps (30 min in PBS followed by immersion in PBS containing 30% sucrose) were followed over 12 hrs period at 4 °C. After the washing steps, the tissue samples were embedded in OCT (Tissue Tek) and then cryosectioned to thin (5 µm thickness) tissue specimens.

2.3. Picrosirius red staining

Mouse heart sections were incubated in distilled water for 5 minutes, followed by 2% phosphomolybdic acid solution for 20 minutes, and picrosirius red solution (0.1% in saturated picric acid) for 90 minutes. The slides were rinsed twice in quick succession using 5% acetic acid (in ddH_2O). Then the sections were dehydrated three times with anhydrous alcohol (3 minutes per rinse), cleared with xylene two times (3 minutes per rinse), and mounted in polymount xylene. Images were captured using Leica DM6 B upright microscope equipped with Leica DFC450 color CCD under bright-field imaging mode as well as using polarized light microscopy to detect picrosirius red enhanced birefringence from the fibrillar collagen.

2.4. Immunohistochemical (IHC) collagen staining

Mouse heart sections were incubated in blocking buffer (5% goat serum, 0.1% Triton X-100, 2% BSA, and 0.1% sodium azide in TBS) solution for one hour at room temperature. Then the blocked sections were incubated overnight at 4°C with the antibodies anti-Col1 (Abcam, ab34710, 1:100) or anti-Col3 (Abcam, ab7778, 1:100)) diluted in a blocking buffer solution

Biomedical Optics EXPRESS

while each labeling was done separately in a series of specified MI time points. The slides were rinsed thrice in TBS containing 0.1% Triton X100, followed by incubation with goat anti-rabbit coupled dyes (Alexa Fluor 647 and/or Alexa Fluor 555; 1:500 dilution) for 1 hour at room temperature. The slides were stored for further processing by putting mounting media on it. The fluorescence imaging was performed using a confocal microscope (Leica Microsystems). For each experimental group, the number of samples were at least 2.

2.5. Multiphoton imaging

SHG and two-photon microscopy were performed on a Leica SP5 resonant scanning multiphoton confocal inverted microscope (with a tunable pulsed laser $\lambda = 690$ - 1040 nm). For all the SHG imaging, an excitation wavelength of 860 nm with a pulse width of 70 fs at 84 MHz repetition rate were utilized. The laser pulses were focused onto the tissue specimen through a 10x, 0.40 NA air objective (Obj. HC PL APO 10x/0.40 CS, Leica) in noncontact imaging mode. The SHG emission was collected in the backward direction using the same objective by selecting a filter cube (680 nm short pass filter) equipped with 320–435 nm range band pass filter (> 90% transmission). The two-photon fluorescence signals from the tissue was collected through 486–506 nm narrow range band-pass filter and detected by non-descanned modular type photomultiplier tubes (PMT) detectors. Typical laser power measured is about 100 mW at the objective focus during SHG imaging. LAS X software (Leica Microsystems) was employed for controlling the laser scanning, and image acquisition. Image sizes were of 1024 x 1024 pixels captured at 400 Hz scan speed per line giving a pixel dwell time of 2.44 µs per pixel. For colocalization studies in the infarcted region, 25x, 0.95 NA water objective lens (HC FLUOTAR L 25x/0.95. W VISIR, Leica) was used. In this paper, SHG and two-photon fluorescence are represented as pseudo colored pixels, green and red, respectively. 63x, 1.4 NA oil-immersion objective (Obj. HCX PL APO 63x/1.40–0.60 OILCS, Leica) was used to capture the point spread function (PSF) of our microscope using nanoscale $BaTiO_3$ beads as point source of SHG emission. The lateral resolution measured using 10x, 0.40 NA, 25x, 0.95 NA and 63x, 1.4 NA objectives are 2.13 µm, 1.05 µm and 0.43 µm respectively using sub-diffraction $BaTiO_3$ nanoparticles.

2.6. Image processing and statistical data analysis

SHG image analysis were performed in ImageJ software (NIH, Bethesda, MD). Image segmentation and thresholding operation on the pixels were performed for the quantitative analysis of the images. Regional and global collagen percentages were quantitatively determined by calculating the fraction of pixels with SHG signal (green pixels) to total sum of pixels containing both green and red pixels. Colocalization rate analysis were performed using Leica LASX Imaging Software module. Collagen fiber dimensions such as length, thickness and fiber orientation were extracted using open source CT-FIRE program [41]. Statistical significance of the data was determined employing Student's t-test and showed as mean ± standard deviation of the mean.

3. Results and discussion

Figure S1a-c schematic depicts the characterization of mouse model following MI. We successfully induced MI in mice model following surgical ligation of left coronary artery just below the left atrium, which was later confirmed by echocardiography (Figure S1k) and multiphoton SHG imaging of the heart sections.

MI injury is followed by extraction, slicing of hearts, and fixation of thin (~ 5 µm) tissue sections for structural characterization and quantification of extracellular matrix (ECM) proteins at different time points (Figure S1b, S1c). We first determined the 2D and 3D point spread function (PSF) of our SHG microscope (Figure S1d-h) employed for imaging collagen fibers. The PSF is usually calculated from the full-width-half-maximum (FWHM) of the emission spectra of the SHG light source. The PSF of the SHG microscope was measured using a 100 nm

Biomedical Optics EXPRESS

$BaTiO_3$ nanoparticles as point source of SHG emitters. TEM analysis (Figure S1i) showed that the nanoparticles are predominantly spherical with an average diameter of 100 nm ± 5 nm. Figure S1f-h show the xy, yz and xz image plane of a single nanoparticle obtained using 820 nm excitation light with a 63x oil-immersion objective lens with numerical aperture of 1.40. A linescan illustrating the intensity profile xy and yz image plane of the bead is shown in Figure S1d and S1e respectively. The intensity profile was fitted using a Gaussian function and the full-width-half-maximum (FWHM) of the fit provides the resolution in respective planes along transverse and longitudinal or axial direction. From these measurements, the xy resolution was found to be 430 nm and the yz resolution was found to be ~ 1.3 µm. To characterize the penetration depth provided by the microscope, 100 nm $BaTiO_3$ beads were dispersed in 1.5% agarose gel medium. The SHG images were recorded at z = 0.29 µm intervals and z-stack collected was combined to form the 3D image, processed using Imaris software (Figure S1j). The depth dependence of SHG signal was obtained by plotting the SHG intensity from the bead along the depth of gel. The SHG intensity was found to decrease with increase of depth away from the objective focus and the range of the scattering length was roughly estimated around ~ 150 µm using the nanoscale beads in the agarose gel. To elucidate the alterations in the 2D organization of collagenous ECM proteins in the heart tissues during the progression of MI, we analyzed brightfield and polarization microscopy images of picrosirius red (PSR) stained cardiac histological sections, where collagen looks red in PSR images. The results shown in Fig. 1(a) clearly displayed a progressive deposition of collagen in the LV region over the period of 4 weeks. The collagen deposition was accompanied with thinning of left ventricular wall, and the dilation of the ventricular area. From PSR transmitted light microscopy images (Fig. 1(b)), we observed significant increase in collagen complexity between 1 and 2 weeks. Picrosirius red dye stains both types of fibrillar collagen I and III, hence provide total collagen information. By image segmentation and simple threshold pixel counting method (Figures S2-S6), we quantified the fraction of red pixels in PSR images of whole heart tissues as well as highly sensitive infarct regions of left ventricle region at different time points, after MI injury. While we do not see any significant variation in collagen expression up to 4 days, by day 5–6 we observed substantial deposition of collagen (Figure S7). Also, using polarized light microscopy, we characterized picrosirius red enhanced birefringence detection from collagen fibrils in range of colors from weak green to yellowish orange depending on density and 3D orientation of collagen fibers (Figs. 1(c) and S8). The results at specific time points were consistent in SHG, brightfield and polarization microscopy images. The progression of fibrosis and collagen maturation with increasing density of fibrillar collagens were clearly observed in the infarct zone after one week and beyond.

In order to further characterize fibrosis of heart and visualize the alterations in the collagenous extracellular matrix protein levels from early to late stages after MI-injury, we imaged the cardiac tissue sections simultaneously using both two-photon fluorescence and SHG microscopy. SHG provides signal from collagen fibers while two photon fluorescence originates from endogenous cellular chromophores that is primarily attributed to FAD present in the cardiac cells [42,43]. SHG images provide a high-resolution signature (green pixels) of network of collagen fibers due to the highly ordered fibrillar collagens (type I and type III) (Fig. 1). The red pixels represent the autofluorescence from the cardiomyocytes due to two-photon excitation and originating without any exogenous labeling. The SHG signal observed is primarily contributed by collagen type I and type III fibers, which is highly sensitive to alignment of fibers with respect to light polarization, also seen by other researchers using polarization-resolved SHG measurements [44]. Additionally, post-MI, the area covered by the two-photon excited autofluorescence (represented by red pixels in the image), progressively decreased over time. This is due to the death of cardiomyocytes and lack of their regeneration therein. Further, the dead cardiomyocytes are being gradually replaced by collagenous scar tissues with the progression of fibrosis. We note that after 2 to 4

Biomedical Optics EXPRESS

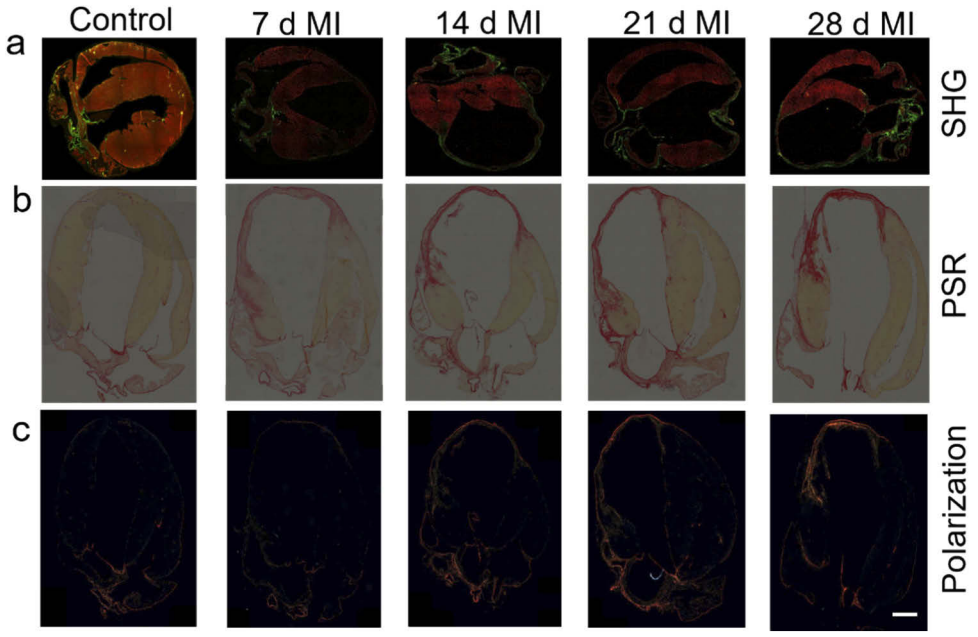

Fig. 1. Progression of scar formation after MI in the mouse heart. (a) Overlayed SHG (green) and two-photon autofluorescence (red) images at different time points showing the deposition of collagen after MI. 10x, 0.4 NA objective lens was used to capture these images. For comparison, (b) bright field images of the picrosirius red (PSR) stained, and (c) birefringence detection using polarized light for heart tissues collected from the same time points are shown. Scale bar: 500 µm

weeks, the cardiomyocytes were entirely replaced by fibrillar collagen at the LV region of the infarcted scar zone (Fig. 1). We also recorded the SHG emission spectra from the infarcted scar region under two photon excitation of 860 nm (in the visible region of 390–780 nm) (Fig. 2(c)). As seen from Fig. 2(c), the spectrum is primarily dominated by sharp SHG signal at 430 nm from the collagenous scar tissue and relatively weak broad two photon autofluorescence across the visible region of the spectrum. The corresponding SHG image is shown in Fig. 2(d). The ratio of cardiomyocytes (autofluorescence signals) to collagen (SHG signals) would represent the healthiness of cardiac tissues. Therefore, the ratio of SHG area and TPF channel area has been implemented in this study to calculate the extent of fibrosis. These fibrosis scoring methodology was previously implemented in various other disease models [45–47].

High resolution SHG images from the LV region were further utilized to examine the microscopic morphological changes following MI. Figure 2(a) shows the variation of LV wall thickness with the progression of time after MI. The LV wall thickness decreased from 1.43 ± 0.2 mm for the control group to 0.45 ± 0.06 mm at 1 week after MI, a 3-fold decrease; it further reduced to 0.22 ± 0.02 mm at 2 weeks, and to 0.17 ± 0.02 mm at 4 weeks' time point. Figure 2(b) shows the LV dilation at different time points after MI. We measured 1.8, 2.7, 2.6-times increase of LV diameter after 3 days, 5 days and 7 days post MI. The maximum LV dilation of up to 3.7-fold increase compared to the sham groups were measured in the 2 to 4 weeks post MI groups. We also detected significant increase in collagen fiber deposition after 2 to 4 weeks post-MI during scar remodeling, which contribute to large increase in stiffness of the ventricular wall accompanied by thinning of LV and increased ventricular dilation. For closer examination of increased fibrosis in LV during ECM remodeling, we analyzed other morphological features such as fiber length, fiber thickness and their orientation. The fiber orientations were characterized

Biomedical Optics EXPRESS

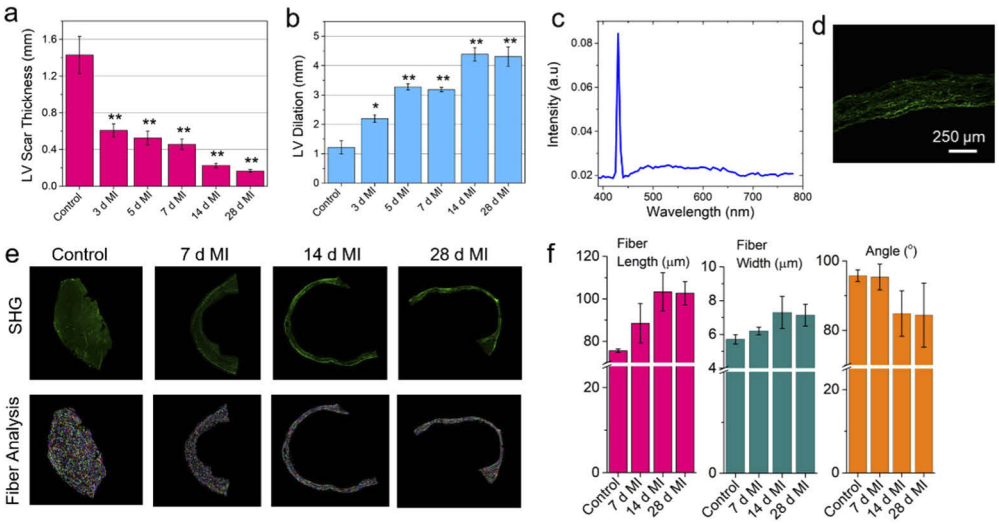

Fig. 2. Evaluation of MI size and assessment of cardiac fiber characteristics post MI in the left ventricle. (a) Quantification of LV wall thickness at different time points compared to sham (control) group using the SHG images. (b) Assessment of LV dilation with respect to septum at different time points after MI injury using the SHG images. (c) SHG spectrum collected from the scar region post 4 week-MI. (d) The corresponding SHG image of the scar region. (e) Representative SHG image (top panel) of the LV region after 7, 14, and 28 days post MI compared to the sham group. The corresponding cardiac fiber analysis for each image is shown in the bottom panel. (f) The variation of estimated fiber length, fiber width, and fiber inclination angle at different time points post MI using the SHG images acquired using 10x, 0.4 NA objective lens. Scale bar 250 µm. *$p < 0.05$, **$p < 0.001$, one-way ANOVA

by the helix pitch angle, and their alignment in the SHG images. We calculated the cardiac fiber characteristics in the healthy and infarcted heart tissues (Figures S9, S10) at specified time points using the program CT-FIRE [48,49]. While the healthy hearts displayed sparse arrangement of relatively smaller collagen fibers of ~ 76 µm in length, infarcted hearts showed significantly longer, dense collagen fibers approaching ~ 103 µm and ~ 100 µm in length after 2 weeks and 4 weeks post MI, respectively, showing more than 30% increase in fiber length (Figs. 2(e), 2(f)). These results also support the stronger SHG signatures observed earlier in the infarcted mouse heart samples. This is due to the dense network of collagen fibers and long-range coherent quasi-crystalline order in relatively longer elongated collagen fibers that would result in strong SHG signals, consistent with the increased SHG signals in the infarcted mouse hearts (Fig. 1(a)). The characterization of the cardiac fiber widths showed up to ~ 25% increase in the fiber diameter (Fig. 2(f)) in the infarcted tissues compared to the sham group. This is due to increased cross-linked assembly of collagen fibrils in the infarcted tissues relative to healthy heart tissues.

To confirm the origin of SHG signals, we used Alexa-647 labeled anti-collagens on our tissue samples to simultaneous capture SHG and fluorescence images. We selected Alexa-647 dyes to make sure the emitted fluorescence signals do not interfere with the SHG signals (Figure S11). Overlay images composing the fluorescence and SHG channels allow one to generate estimates of colocalization of pixels. Image colocalization analysis between fluorescence channel and SHG channel was performed using the Leica image processing software equipped with colocalization plugin to analyze for colocalization rate, Pearson correlation and overlap coefficient between the fluorescence-antibodies labeled collagens (anti-collagens) and SHG channel. The colocalization

Biomedical Optics EXPRESS

rate value refers to the degree of colocalization in % and is determined from the ratio of the area of colocalizing signals (colocalization area) and foreground area (where foreground area = area of the image/area of the background). The overlap coefficient indicates the overlap of the signals in both color channels and thus, the extent of colocalization. Pearson correlation coefficient describes the strength of the correlation between the gray-scale value distribution in the first color channel and that in the second color channel and indicates the extent to which the displays in both color channels match.

Using the permanent ligated MI model we have shown in this study that SHG can be utilized as a robust and label-free tool to assess cardiac fibrosis dynamically at different time points post MI. Fibrosis of LV region was evident from the exponential growth of collagen concentration (Fig. 3(a), (b)) from 1 day to 4 weeks after MI compared to the control group. We observed ~ 8-fold increase of collagen deposition in the global (whole heart) compared to healthy control heart (without MI) (Fig. 3(a), 3(b)). Furthermore, we observed 12.7-, 14.8-, 18.5- and 16.3-times increase of collagen deposition compared to sham (control) group after 1, 2, 3- and 4-weeks post-MI, respectively (Fig. 3(a), 3(b)). Previous study from Fu et al. [21] also showed non-linear increase of cardiac fibroblast dynamics post MI. In addition, SHG can provide high-resolution ~ 430 nm lateral resolution (Figure S1d) images. Parallel studies using picrosirius red showed a similar, albeit a slightly larger, overall increase in collagen deposition compared to SHG results (Fig. 3(c), (d)). Previous study indicated picrosirius red slightly over predicts the level of fibrosis [50]. This is because the histological stain does not differentiate between fibrillary and non-fibrillary collagen networks [51]. In contrast, SHG signal is highly specific to fibrillar collagen type I and type III and does not come from non-fibrillar collagen type IV [30]. Therefore, SHG provides improved specificity and accurate analysis of progression of fibrosis in diseased heart. Even immunolabeling is prone to error as it is dependent on the recognition capability of antibodies to the accessible epitopes.

Figure 4(a)–(c) show the fluorescence, SHG, and the colocalization images. Figure 4(d) shows gradual increase in colocalization rate between SHG channel and immunofluorescence channel as a function of days after MI. The results are consistent with the increase in the density of fibrillar collagens in scar tissue and scar maturation which would produce more collagen type I. The analysis also suggests that the SHG signal (represented by green pixels) colocalize better with immunofluorescence (red pixels) labeled with anti-Col1 than anti-Col3 (Fig. 4(a)–(d)) particularly marked with increase in collagen deposition. Thus, both the colocalization analysis (Figures S12-S14) and the Pearson analysis (Figs. 4(d), 4(e)) support the conclusion that the SHG signal is primarily generated from collagen type I isoform. The overlap coefficient (Fig. 4(f)) showed slightly lower overlap for anti-Col3 compared to anti-Col1.

In order to extract the dynamics of Col1 and Col3 expression levels and their ratio in the infarcted myocardium, we further performed the immunofluorescence experiments with another dye labeled antibodies. We conjugated Alexa 555-labeled collagen 1 antibodies (anti-Col1) and collagen 3 antibodies (anti-Col3) to specific collagen types. As a control, we used unlabeled tissue sections. Representative fluorescence images are shown in Figure S11. Figure 5(a) shows 1.8-, 4.2 and 4.16 fold increase of Col1 fluorescence intensity compared to the sham group. The increase of Col1 level was found to be statistically significant with $p < 0.05$ using one-way ANOVA analysis. The dynamics of Col 3 fluorescence intensity showed similar trend (Fig. 5(b)). Figure 5(c) shows the kinetics of the ratio of Col1/Col3 over four weeks post-MI. Therein, the normalized ratio of Col1/Col3 expression appears to be quite similar without any meaningful changes up to 1 week post-MI; Col1/Col3 ratio was found to be increased at later time points (2 - 4 weeks) after MI injury. These results suggested pronounced concentration of collagen I expression in the LV scar zone at 2- and 4-weeks post MI and also consistent with our SHG imaging results (Fig. 1 and Fig. 3(b)). Further, Fig. 5(c) results indicated that Col3 expression is upregulated first, followed by Col1 expression during the course of MI. Finally, the

Biomedical Optics EXPRESS

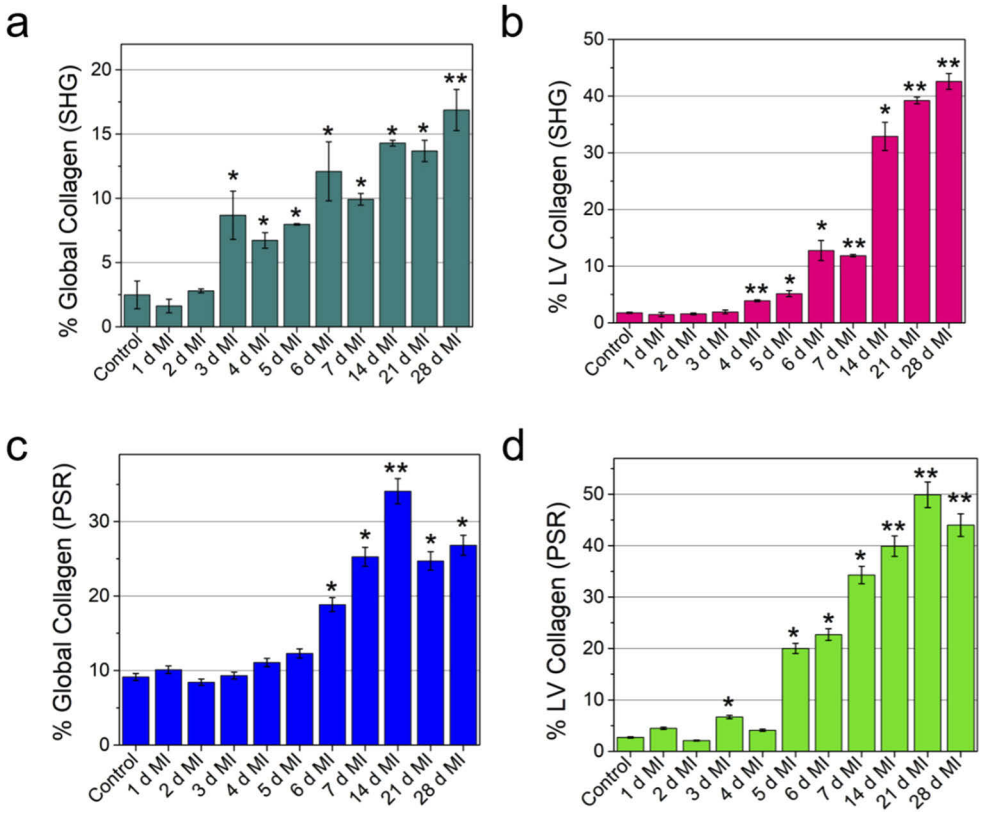

Fig. 3. Global (whole heart) and local (LV region) quantification of collagen deposition showing the progression of fibrosis after MI. Quantification of collagen deposition using SHG images (a) calculated from whole heart, (b) calculated from the LV region. Quantification of collagen deposition using picrosirius red staining (c) calculated from whole heart, (d) calculated from the LV region. The collagen percentage was calculated as the ratio of the area occupied by the collagen to the total area of the tissue (a, c) or the area occupied by the collagen to the area of the LV region (b, d). For each time point the collagen percentage were averaged over two separate heart sections. Heart from separate mice were used for each time point. SHG and PSR imaging were performed on heart tissue collected from separate mice. *$p < 0.05$, **$p < 0.001$, one-way ANOVA.

Biomedical Optics EXPRESS

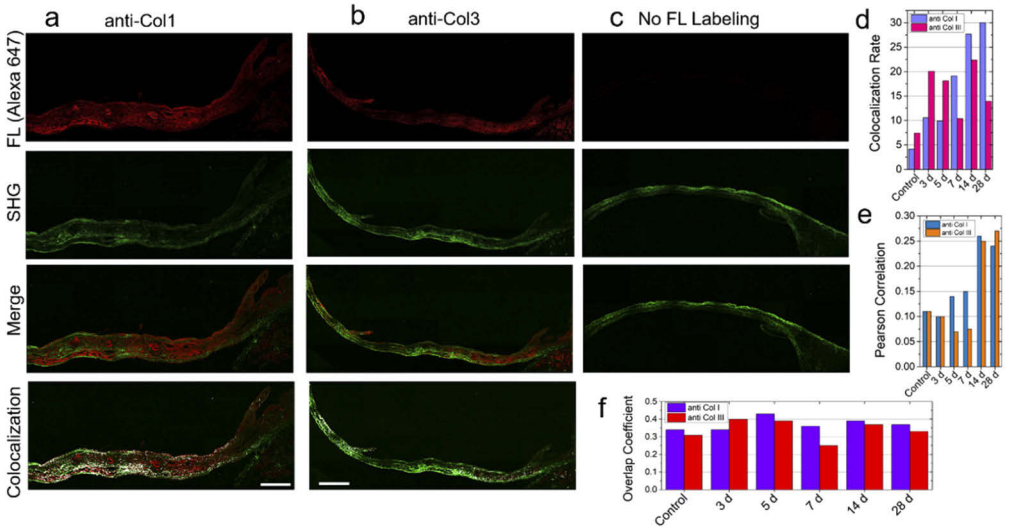

Fig. 4. Comparison of immunohistochemistry (IHC) and SHG imaging after MI. Representative image of Alexa647-labeled (a) collagen type I (anti-col1), (b) collagen type III antibodies (anti-col3), and (c) no fluorescence in heart tissue section post 4 week (28 d) of MI injury. The SHG images of the same tissue immunolabeled with anti-col1 and anti-col3 are shown in the second panel under a-c captured employing 25x, 0.95 NA water objective lens. The overlap images of the fluorescence and SHG are shown in the third panel under a-c. The colocalization analysis of the SHG and fluorescence images are shown in the fourth panel. (d) Colocalization rate, (e) Pearson correlation coefficient, and (f) Overlap coefficient comparing anti-col1 and anti-col3 at different time points after MI. Scale bar: 250 µm.

comparison of progression of SHG channel and immunofluorescence signal as a function of days after MI showed similar trend (Fig. 5(d)) validating our measurements and also consistent with documented literature reports [52–55].

Fibroblasts in the cardiac tissues produce the procollagen strands. Three procollagen strands come together to form the triple helical structure of the procollagen with an N- and C-terminal propeptide at each end. When the procollagen are transported from the fibroblasts into the intracellular spaces, the propeptides are cleaved to form collagen. When matured, the collagen forms large cross-linked fibrillary structures and is embedded in the collagen network of the heart [56]. The SHG signal mostly comes from the triple helix (~ 300 kD) structure of the collagen. Each collagen I molecule is composed of two α1 and one α2 while each collagen III molecule is composed of three α1 chains. These alpha chains differ in terms of their charge distributions, pitch angle, and the angle made by the helical coil with respect to the linear axis of the protein [57–59]. It is also known from their structures that type I and type II collagen fibers give most intense SHG signals while collagen type III fibers shows weak SHG signals [32]. Studies have found that the fraction of collagen III to collagen I plays a major role in diseases involving cardiac fibrosis and cardiomyopathy [60]. Thus, resolving distribution of collagen isoforms and their precise quantification will be very important for understanding how the collagen I/III balance alters the progression of heart disease and related diagnostics. Some approaches to differentiate collagen types that have been pursued in the past included HPLC coupled with mass spectrometry [61] which is not practical for widespread use, conventional fluorescence labeling of tissues [51] which however usually suffers from unspecific labeling and reproducibility issues, fluorescence lifetime imaging microscopy (FLIM) [58] and polarization-resolved SHG image analyses [59]. For example, Tilbury et.al developed polarization-resolved SHG image analyses

Biomedical Optics EXPRESS

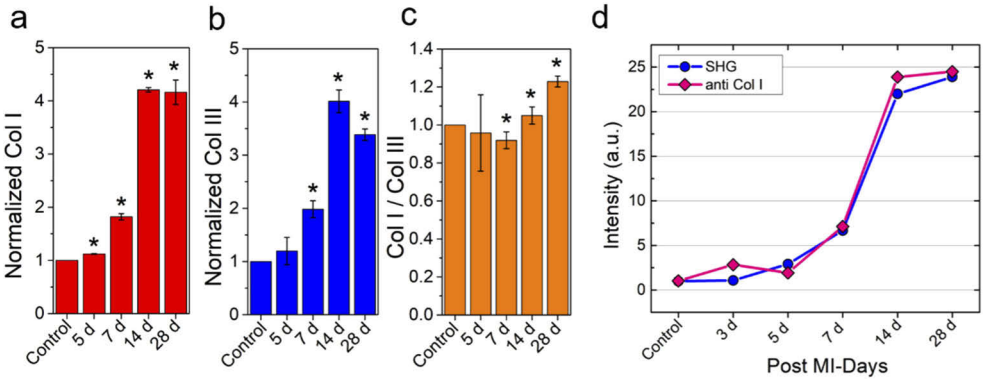

Fig. 5. Time-dependent distribution of different isoforms of myocardial collagen after MI. (a) Normalized collagen type I expression with respect to uninjured hearts at different time points after MI. (b) Normalized collagen type III contents with respect to uninjured heart at different time points post-MI. (c) ratio of Col I to Col III distribution during the course of progression of fibrosis monitored over 4 weeks' time period. (d) Comparison of variation of SHG and fluorescence signal as a function of days after MI showing a good correlation between SHG and immunohistochemistry studies. For each time period, two separate heart sections were analyzed. *$p < 0.05$, one-way ANOVA.

to differentiate collagen I and III [59]. Their measurements showed that increased collagen III led to more randomized tissue due to the decrease in the alignment of dipole moments within collagen fibrils [59]. Ranjit et.al combined SHG with fluorescence lifetime imaging technique and phasor approach to distinguish collagen I and III [58]. These techniques were mostly applied in preformed collagen gels/or mixtures while requiring sophisticated optical set ups to obtain multimodal imaging data sets, including complex image analysis methods, but largely provided qualitative information on separation of collagen types [58,59]. Hence, developing robust SHG imaging approaches for not only resolving collagen isoforms but also their quantitative characterization in tissues is warranted for understanding various disease models involving fibrosis. Moreover, biomedical imaging and associated medical diagnosis will further advance with developments in deep learning-based image processing algorithms which could potentially enable automated scoring of fibrosis stages in organs as already demonstrated by researchers in liver, lung and heart disorder [40,62–64].

Other advantages of the SHG technique include the potential to use it *in vivo*. Recently multiphoton microendoscopy [65–69] probes have been utilized to image contraction of single motor unit in amyotrophic lateral sclerosis (ALS) mouse [70], high speed imaging of sarcomere in human [71,72], mouse kidney [69], and margin diagnosis of early gastric cancer [73]. In future, microendoscopy based SHG probe could be developed to visualize and assess heart tissues for collagen deposition and fibrosis.

4. Conclusion

In summary, we utilized endogenous signal from collagen using label-free SHG microscopy to quantify the progression of fibrosis in a mouse MI model. The structural assessment of cardiac fibers such as fiber length, width, number of fibers and arrangement of fibers post-MI were quantitatively determined from the analysis of SHG images. Using post-mortem analysis of cardiac tissues, the SHG imaging results were validated against traditional picrosirius red staining and immunofluorescence imaging of antibodies labeled tissues. The progression of fibrosis were characterized from the distribution of collagen isoforms and structural parameters post-MI injury.

Biomedical Optics EXPRESS

Colocalization rate analysis using correlative fluorescence imaging of antibody stained collagen isoforms and SHG microscopy from the left ventricular infarcted scar area showed that the SHG signal is primarily originating from collagen type I structure. This study showed that SHG is an improved, robust, and label-free technique to accurately quantify collagen deposition in cardiac tissue. Further, SHG imaging can be applied as a screening tool for understanding the mechanism of fibrosis and discovery of new therapeutics for fibrosis to improve outcomes in patients with MI.

Funding. National Institutes of Health (5P30GM118430-05, 1P20GM135002-01, 1P30-DK072476); Louisiana Board of Regents (LEQSF(2017-20)-RD-A-04).

Acknowledgments. The project/work used (Genomics or Cell Biology & Bioimaging) core facilities that are supported in part by COBRE (5P30GM118430-05, 1P20GM135002-01) and NORC (P30DK072476) center grants from the National Institutes of Health. M.R.G. thanks the support from LSU start-up fund, Louisiana Board of Regents Support Fund (RCS Award Contract Number: LEQSF(2017-20)-RD-A-04).

Disclosures. The authors declare no conflicts of interest.

See Supplement 1 for supporting content.

References

1. D. Mozaffarian, E. J. Benjamin, A. S. Go, D. K. Arnett, M. J. Blaha, M. Cushman, S. de Ferranti, J.-P. Després, H. J. Fullerton, and V. J. Howard, "American heart association statistics committee and stroke statistics subcommittee," Circulation **141**(9), e29–e322 (2020).
2. V. L. Roger, A. S. Go, D. M. Lloyd-Jones, R. J. Adams, J. D. Berry, T. M. Brown, M. R. Carnethon, S. Dai, G. De Simone, and E. S. Ford, "Heart disease and stroke statistics-2011 update: a report from the American Heart Association," Circulation **123**(4), e18–e209 (2011).
3. B. I. Jugdutt, "Ventricular remodeling after infarction and the extracellular collagen matrix: when is enough enough?" Circulation **108**(11), 1395–1403 (2003).
4. G. Ertl and S. Frantz, "Healing after myocardial infarction," Cardiovasc. Res. **66**(1), 22–32 (2005).
5. B. I. Jugdutt, "Aging and remodeling during healing of the wounded heart: current therapies and novel drug targets," Curr. Drug Targets **9**(4), 325–344 (2008).
6. K. T. Weber, R. Pick, J. E. Jalil, J. S. Janicki, and E. P. Carroll, "Patterns of myocardial fibrosis," J. Mol. Cell. Cardiol. **21**, 121–131 (1989).
7. J. S. Janicki and G. L. Brower, "The role of myocardial fibrillar collagen in ventricular remodeling and function," J. Card. Fail. **8**(6), S319–S325 (2002).
8. B. López, A. González, S. Ravassa, J. Beaumont, M. U. Moreno, G. San José, R. Querejeta, and J. Díez, "Circulating biomarkers of myocardial fibrosis: the need for a reappraisal," J. Am. Coll. Cardiol. **65**(22), 2449–2456 (2015).
9. K. T. Weber, Y. Sun, L. C. Katwa, J. P. Cleutjens, and G. Zhou, "Connective tissue and repair in the heart: potential regulatory mechanisms," Ann. N. Y. Acad. Sci. **752**(1), 286–299 (1995).
10. K. T. Weber, "Cardiac interstitium in health and disease: the fibrillar collagen network," J. Am. Coll. Cardiol. **13**(7), 1637–1652 (1989).
11. M. R. Zile, C. F. Baicu, J. S. Ikonomidis, R. E. Stroud, P. J. Nietert, A. D. Bradshaw, R. Slater, B. M. Palmer, P. Van Buren, and M. Meyer, "Myocardial stiffness in patients with heart failure and a preserved ejection fraction: contributions of collagen and titin," Circulation **131**(14), 1247–1259 (2015).
12. T. Yamada, M. Fukunami, M. Ohmori, K. Iwakura, K. Kumagai, N. Kondoh, T. Minamino, E. Tsujimura, T. Nagareda, and K. Kotoh, "Which subgroup of patients with dilated cardiomyopathy would benefit from long-term beta-blocker therapy? A histologic viewpoint," J. Am. Coll. Cardiol. **21**(3), 628–633 (1993).
13. L. T. Cooper, K. L. Baughman, A. M. Feldman, A. Frustaci, M. Jessup, U. Kuhl, G. N. Levine, J. Narula, R. C. Starling, and J. Towbin, "The role of endomyocardial biopsy in the management of cardiovascular disease: a scientific statement from the American Heart Association, the American College of Cardiology, and the European Society of Cardiology Endorsed by the Heart Failure Society of America and the Heart Failure Association of the European Society of Cardiology," J. Am. Coll. Cardiol. **50**(19), 1914–1931 (2007).
14. P. Elliott and E. Arbustini, "The role of endomyocardial biopsy in the management of cardiovascular disease: a commentary on joint AHA/ACC/ESC guidelines," Heart **95**(9), 759–760 (2009).
15. C. Chimenti and A. Frustaci, "Contribution and risks of left ventricular endomyocardial biopsy in patients with cardiomyopathies: a retrospective study over a 28-year period," Circulation **128**(14), 1531–1541 (2013).
16. F. Sweat, H. Puchtler, and S. I. Rosenthal, "Sirius red F3BA as a stain for connective tissue," Arch. Pathol. **78**, 69–72 (1964).
17. L. Junqueira, W. A. Cossermelli, and R. Brentani, "Differential staining of collagens type I, II and III by Sirius Red and polarization microscopy," Arch. Histol. Jpn. **41**(3), 267–274 (1978).
18. P. Whittaker, R. Kloner, D. Boughner, and J. Pickering, "Quantitative assessment of myocardial collagen with picrosirius red staining and circularly polarized light," Basic Res. Cardiol. **89**(5), 397–410 (1994).

Biomedical Optics EXPRESS

19. Y. Zhang, X. Wu, Y. Li, H. Zhang, Z. Li, Y. Zhang, L. Zhang, J. Ju, X. Liu, and X. Chen, "Endothelial to mesenchymal transition contributes to arsenic-trioxide-induced cardiac fibrosis," Sci. Rep. **6**(1), 1–12 (2016).
20. F. Ma, Y. Li, L. Jia, Y. Han, J. Cheng, H. Li, Y. Qi, and J. Du, "Macrophage-stimulated cardiac fibroblast production of IL-6 is essential for TGF β/Smad activation and cardiac fibrosis induced by angiotensin II," PLoS One **7**(5), e35144 (2012).
21. X. Fu, H. Khalil, O. Kanisicak, J. G. Boyer, R. J. Vagnozzi, B. D. Maliken, M. A. Sargent, V. Prasad, I. Valiente-Alandi, and B. C. Blaxall, "Specialized fibroblast differentiated states underlie scar formation in the infarcted mouse heart," J. Clin. Investig. **128**(5), 2127–2143 (2018).
22. A. S. Flett, J. Hasleton, C. Cook, D. Hausenloy, G. Quarta, C. Ariti, V. Muthurangu, and J. C. Moon, "Evaluation of techniques for the quantification of myocardial scar of differing etiology using cardiac magnetic resonance," JACC: Cardiovascular Imaging **4**(2), 150–156 (2011).
23. S. Angeli, N. Befera, J.-M. Peyrat, E. Calabrese, G. A. Johnson, and C. Constantinides, "A high-resolution cardiovascular magnetic resonance diffusion tensor map from ex-vivo C57BL/6 murine hearts," J Cardiovasc Magn Reson **16**(1), 77 (2014).
24. X. Qin and B. Fei, "DTI template-based estimation of cardiac fiber orientations from 3D ultrasound," Med. Phys. **42**(6Part1), 2915–2924 (2015).
25. C. J. Goergen, H. H. Chen, S. Sakadžić, V. J. Srinivasan, and D. E. Sosnovik, "Microstructural characterization of myocardial infarction with optical coherence tractography and two-photon microscopy," Physiol. Rep. **4**(18), e12894 (2016).
26. S. R. Watson, J. D. Dormer, and B. Fei, "Imaging technologies for cardiac fiber and heart failure: a review," Heart Failure Rev. **23**(2), 273–289 (2018).
27. Q. Yu and A. A. Heikal, "Two-photon autofluorescence dynamics imaging reveals sensitivity of intracellular NADH concentration and conformation to cell physiology at the single-cell level," J. Photochem. Photobiol., B **95**(1), 46–57 (2009).
28. A. Zoumi, X. Lu, G. S. Kassab, and B. J. Tromberg, "Imaging coronary artery microstructure using second-harmonic and two-photon fluorescence microscopy," Biophys. J. **87**(4), 2778–2786 (2004).
29. P. S. Gade, A. M. Robertson, and C. Y. Chuang, "Multiphoton imaging of collagen, elastin, and calcification in intact soft-tissue samples," Curr. Protoc. Cytm. **87**(1), e51 (2019).
30. P. Campagnola, "Second harmonic generation imaging microscopy: applications to diseases diagnostics," Anal. Chem. **83**(9), 3224–3231 (2011).
31. I. Freund, M. Deutsch, and A. Sprecher, "Connective tissue polarity. Optical second-harmonic microscopy, crossed-beam summation, and small-angle scattering in rat-tail tendon," Biophys. J. **50**(4), 693–712 (1986).
32. X. Chen, O. Nadiarynkh, S. Plotnikov, and P. J. Campagnola, "Second harmonic generation microscopy for quantitative analysis of collagen fibrillar structure," Nat. Protoc. **7**(4), 654–669 (2012).
33. L. Mostaço-Guidolin, N. L. Rosin, and T.-L. Hackett, "Imaging collagen in scar tissue: developments in second harmonic generation microscopy for biomedical applications," Int. J. Mol. Sci. **18**(8), 1772 (2017).
34. A. Zoumi, A. Yeh, and B. J. Tromberg, "Imaging cells and extracellular matrix in vivo by using second-harmonic generation and two-photon excited fluorescence," Proc. Natl. Acad. Sci. **99**(17), 11014–11019 (2002).
35. W. R. Zipfel, R. M. Williams, and W. W. Webb, "Nonlinear magic: multiphoton microscopy in the biosciences," Nat. Biotechnol. **21**(11), 1369–1377 (2003).
36. E. Brown, T. McKee, A. Pluen, B. Seed, Y. Boucher, and R. K. Jain, "Dynamic imaging of collagen and its modulation in tumors in vivo using second-harmonic generation," Nat. Med. **9**(6), 796–800 (2003).
37. S. P. Sahu, A. Mahigir, B. Chidester, G. Veronis, and M. R. Gartia, "Ultrasensitive three-dimensional orientation imaging of single molecules on plasmonic nanohole arrays using second harmonic generation," Nano Lett. **19**(9), 6192–6202 (2019).
38. J. Liu, I.-H. Cho, Y. Cui, and J. Irudayaraj, "Second harmonic super-resolution microscopy for quantification of mRNA at single copy sensitivity," ACS Nano **8**(12), 12418–12427 (2014).
39. J. Butet, P. Brevet, and O. Martin, "Optical second harmonic generation in plasmonic nanostructures: from fundamental principles to advanced applications," ACS Nano **9**, 10545–10562 (2015).
40. Q. Liu, S. Mukhopadhyay, M. X. B. Rodriguez, X. Fu, S. Sahu, D. Burk, and M. Gartia, "A one-shot learning framework for assessment of fibrillar collagen from second harmonic generation images of an infarcted myocardium," in *IEEE 17th International Symposium on Biomedical Imaging (ISBI)* (2020), 41. pp. 839–843.
41. J. S. Bredfeldt, Y. Liu, C. A. Pehlke, M. W. Conklin, J. M. Szulczewski, D. R. Inman, P. J. Keely, R. D. Nowak, T. R. Mackie, and K. W. Eliceiri, "Computational segmentation of collagen fibers from second-harmonic generation images of breast cancer," J. Biomed. Opt. **19**(1), 016007 (2014).
42. W. R. Zipfel, R. M. Williams, R. Christie, A. Y. Nikitin, B. T. Hyman, and W. W. Webb, "Live tissue intrinsic emission microscopy using multiphoton-excited native fluorescence and second harmonic generation," Proc. Natl. Acad. Sci. **100**(12), 7075–7080 (2003).
43. S. Huang, A. A. Heikal, and W. W. Webb, "Two-photon fluorescence spectroscopy and microscopy of NAD (P) H and flavoprotein," Biophys. J. **82**(5), 2811–2825 (2002).
44. K. R. Campbell, R. Chaudhary, J. M. Handel, M. S. Patankar, and P. J. Campagnola, "Polarization-resolved second harmonic generation imaging of human ovarian cancer," J. Biomed. Opt. **23**(06), 1 (2018).

Biomedical Optics EXPRESS

45. L. Gailhouste, Y. Le Grand, C. Odin, D. Guyader, B. Turlin, F. Ezan, Y. Désille, T. Guilbert, A. Bessard, and C. Frémin, "Fibrillar collagen scoring by second harmonic microscopy: a new tool in the assessment of liver fibrosis," J. Hepatol. **52**(3), 398–406 (2010).
46. D. Sevrain, M. Dubreuil, G. E. Dolman, A. Zaitoun, W. Irving, I. N. Guha, C. Odin, and Y. Le Grand, "Evaluation of area-based collagen scoring by nonlinear microscopy in chronic hepatitis C-induced liver fibrosis," Biomed. Opt. Express **6**(4), 1209–1218 (2015).
47. D. C. Tai, N. Tan, S. Xu, C. H. Kang, S. M. Chia, C. L. Cheng, A. Wee, C. L. Wei, A. M. Raja, and G. Xiao, "Fibro-C-Index: comprehensive, morphology-based quantification of liver fibrosis using second harmonic generation and two-photon microscopy," J. Biomed. Opt. **14**(4), 044013 (2009).
48. A. Keikhosravi, Y. Liu, C. Drifka, K. M. Woo, A. Verma, R. Oldenbourg, and K. W. Eliceiri, "Quantification of collagen organization in histopathology samples using liquid crystal based polarization microscopy," Biomed. Opt. Express **8**(9), 4243–4256 (2017).
49. J. S. Bredfeldt, Y. Liu, M. W. Conklin, P. J. Keely, T. R. Mackie, and K. W. Eliceiri, "Automated quantification of aligned collagen for human breast carcinoma prognosis," J. Pathol. Inform. **5**(1), 28 (2014).
50. T. P. Martin, G. Norris, G. McConnell, and S. Currie, "A novel approach for assessing cardiac fibrosis using label-free second harmonic generation," Int. J. Cardiovasc. Imaging **29**(8), 1733–1740 (2013).
51. M. Strupler, A.-M. Pena, M. Hernest, P.-L. Tharaux, J.-L. Martin, E. Beaurepaire, and M.-C. Schanne-Klein, "Second harmonic imaging and scoring of collagen in fibrotic tissues," Opt. Express **15**(7), 4054–4065 (2007).
52. N. Nishikawa, T. Masuyama, K. Yamamoto, Y. Sakata, T. Mano, T. Miwa, M. Sugawara, and M. Hori, "Long-term administration of amlodipine prevents decompensation to diastolic heart failure in hypertensive rats," J. Am. Coll. Cardiol. **38**(5), 1539–1545 (2001).
53. A. M. van der Laan, M. Nahrendorf, and J. J. Piek, "Healing and adverse remodelling after acute myocardial infarction: role of the cellular immune response," Heart **98**(18), 1384–1390 (2012).
54. G. M. Fomovsky and J. W. Holmes, "Evolution of scar structure, mechanics, and ventricular function after myocardial infarction in the rat," Am. J. Physiol. Heart Circ. Physiol. **298**(1), H221–H228 (2010).
55. P. B. Kurnik, M. R. Courtois, and P. A. Ludbrook, "Diastolic stiffening induced by acute myocardial infarction is reduced by early reperfusion," J. Am. Coll. Cardiol. **12**(4), 1029–1036 (1988).
56. E. G. Canty and K. E. Kadler, "Procollagen trafficking, processing and fibrillogenesis," J. Cell Sci. **118**(7), 1341–1353 (2005).
57. M. D. Shoulders and R. T. Raines, "Collagen structure and stability," Annu. Rev. Biochem. **78**(1), 929–958 (2009).
58. S. Ranjit, A. Dvornikov, M. Stakic, S.-H. Hong, M. Levi, R. M. Evans, and E. Gratton, "Imaging fibrosis and separating collagens using second harmonic generation and phasor approach to fluorescence lifetime imaging," Sci. Rep. **5**(1), 13378 (2015).
59. K. Tilbury, C.-H. Lien, S.-J. Chen, and P. J. Campagnola, "Differentiation of Col I and Col III isoforms in stromal models of ovarian cancer by analysis of second harmonic generation polarization and emission directionality," Biophys. J. **106**(2), 354–365 (2014).
60. Y. Yu, G. Yin, S. Bao, and Z. Guo, "Kinetic alterations of collagen and elastic fibres and their association with cardiac function in acute myocardial infarction," Mol. Med. Rep. **17**, 3519–3526 (2017).
61. S. Pataridis, A. Eckhardt, K. Mikulikova, P. Sedlakova, and I. Mikšík, "Identification of collagen types in tissues using HPLC-MS/MS," J. Sep. Sci. **31**(20), 3483–3488 (2008).
62. Y. Yu, J. Wang, C. W. Ng, Y. Ma, S. Mo, E. L. S. Fong, J. Xing, Z. Song, Y. Xie, and K. Si, "Deep learning enables automated scoring of liver fibrosis stages," Sci. Rep. **8**(1), 1–10 (2018).
63. S. Iyengar, X. Li, H. Xu, S. Mukhopadhyay, N. Balakrishnan, A. Sawant, and P. Iyengar, "Toward more precise radiotherapy treatment of lung tumors," Comput. **45**(1), 59–65 (2012).
64. C. Martin-Isla, V. M. Campello, C. Izquierdo, Z. Raisi-Estabragh, B. Baeßler, S. E. Petersen, and K. Lekadir, "Image-based cardiac diagnosis with machine learning: a review," Front. Cardiovasc. Med. **7**, 1 (2020).
65. Y. Zhao, H. Nakamura, and R. J. Gordon, "Development of a versatile two-photon endoscope for biological imaging," Biomed. Opt. Express **1**(4), 1159–1172 (2010).
66. D. R. Rivera, C. M. Brown, D. G. Ouzounov, I. Pavlova, D. Kobat, W. W. Webb, and C. Xu, "Compact and flexible raster scanning multiphoton endoscope capable of imaging unstained tissue," Proc. Natl. Acad. Sci. **108**(43), 17598–17603 (2011).
67. Y. Zhang, M. L. Akins, K. Murari, J. Xi, M.-J. Li, K. Luby-Phelps, M. Mahendroo, and X. Li, "A compact fiber-optic SHG scanning endomicroscope and its application to visualize cervical remodeling during pregnancy," Proc. Natl. Acad. Sci. **109**(32), 12878–12883 (2012).
68. W. Liang, G. Hall, B. Messerschmidt, M.-J. Li, and X. Li, "Nonlinear optical endomicroscopy for label-free functional histology in vivo," Light: Sci. Appl. **6**(11), e17082 (2017).
69. G. Ducourthial, P. Leclerc, T. Mansuryan, M. Fabert, J. Brevier, R. Habert, F. Braud, R. Batrin, C. Vever-Bizet, and G. Bourg-Heckly, "Development of a real-time flexible multiphoton microendoscope for label-free imaging in a live animal," Sci. Rep. **5**(1), 18303–9 (2015).
70. X. Chen, G. N. Sanchez, M. J. Schnitzer, and S. L. Delp, "Microendoscopy detects altered muscular contractile dynamics in a mouse model of amyotrophic lateral sclerosis," Sci. Rep. **10**(1), 1–10 (2020).
71. M. E. Llewellyn, R. P. Barretto, S. L. Delp, and M. J. Schnitzer, "Minimally invasive high-speed imaging of sarcomere contractile dynamics in mice and humans," Nature **454**(7205), 784–788 (2008).

Biomedical Optics EXPRESS

72. G. N. Sanchez, S. Sinha, H. Liske, X. Chen, V. Nguyen, S. L. Delp, and M. J. Schnitzer, "In vivo imaging of human sarcomere twitch dynamics in individual motor units," Neuron **88**(6), 1109–1120 (2015).
73. X. Zheng, N. Zuo, H. Lin, L. Zheng, M. Ni, G. Wu, J. Chen, and S. Zhuo, "Margin diagnosis for endoscopic submucosal dissection of early gastric cancer using multiphoton microscopy," Surg. Endosc. **34**(1), 408–416 (2020).